Available online at www.sciencedirect.com
ScienceDirect
International Journal of Heat and Mass Transfer 50 (2007) 4640–4651
International Journal of HEAT and MASS TRANSFER
www.elsevier.com/locate/ijhmt

Experimental and numerical study of sidewall profile effects on flow and heat transfer inside microchannels

Xiaojin Wei [a], Yogendra Joshi [b,*]

[a] IBM System and Technology, 2070 Route 52, Hopewell Junction, NY 12533, United States
[b] Georgia Institute of Technology, 771 Ferst Drive, Atlanta, GA 30332, United States

Received 18 January 2007; received in revised form 7 March 2007
Available online 23 May 2007

Abstract

The laminar flow characteristics inside slightly tapered silicon microchannels in the hydraulic diameter range of 53–112 μm are investigated. Velocity profiles for planes located at different channel depth are measured using micro resolution particle image velocimetry (micro-PIV). It is revealed that the location of the maximum velocity deviates from the mid-plane along the depth direction due to the wall taper. Numerical simulations are also carried out to examine the effects of the sidewall angle on flow and heat transfer. Large deviation in the velocity profile and consequent significant degradation in heat transfer are observed for considerably tapered microchannels.

Keywords: Microchannel; PIV; Micro-PIV; Laminar flow; Non-ideal geometry; Conjugate heat transfer

0. Introduction

Microchannels are one of the key enabling components of microfluidic devices which have applications ranging from microelectronic cooling to precise drug delivery. Characterizing the transport phenomena inside microchannels is of fundamental importance to the design of these devices. Existing research has focused on measuring bulk transport characteristics such as friction factors or mean thermal resistances for idealized geometries of microtubes [1], rectangular microchannels [2] and trapezoidal microchannels [3]. In reality, due to manufacturing defects, the microchannel profile usually deviates from the ideal geometries assumed. One of the common etching techniques for microchannels is DRIE employing a standard Bosch process, as used in Zhang et al. [4] and Devasenathipathy et al. [5]. Although vertical sidewall is preferred in most cases, sidewall slope as high as 8° was observed [6,7]. This deviation can have important implications on the transport characteristics inside microchannels. It is the objective of this study to investigate this effect through micro-PIV measurements and numerical simulations.

Particle image velocimetry (PIV) is a well-established technique for measuring flow in macro-scale channels. In a typical PIV implementation [8], the flow field to be measured is seeded with flow-tracing particles, which are illuminated with either a pulsed light source or a continuous light source gated by the camera shutter. The images of the particles are taken at two known instants and the displacement of the particle images is then statistically determined by correlation techniques. Significant success has been achieved in developing micro resolution PIV (micro-PIV) systems. The first implementation of micro-PIV was reported in Santiago et al. [9] where an epi-fluorescent microscope was coupled with a continuous Hg-arc lamp and a CCD camera to record the flow around a nominally 30×10^{-6} m elliptical cylinder in a Hele–Shaw flow cell. The resolution of this system was reported to be 6.9×10^{-6} m $\times$ 6.9×10^{-6} m $\times$ 1.5×10^{-6} m. As the time delay between image exposures was controlled through the

* Corresponding author. Tel.: +1 40 4 385 2810; fax: +1 40 4 894 8496.
E-mail addresses: xwei@us.ibm.com (X. Wei), yogendra.joshi@me.gatech.edu (Y. Joshi).

0017-9310/$ - see front matter © 2007 Elsevier Ltd. All rights reserved.
doi:10.1016/j.ijheatmasstransfer.2007.03.020

Nomenclature

d_H	hydraulic diameter (m)
d_p	diameter of the seeding particles for micro-PIV (m)
f	friction factor
$f^{\#}$	f-number for objective lenses
H_c	channel depth (m)
$\bar{h}_x$	longitudinal heat transfer coefficient (W/m^2 K)
k_f	thermal conductivity of the fluid, water in this study (W/m K)
M	magnification of objective lenses
Nu	Nusselt number
$Nu_{conj,bot}$	mean Nusselt number averaged over the bottom wall for conjugate heat transfer
$Nu_{conj,m}$	mean Nusselt number averaged over all peripheral walls for conjugate heat transfer
$Nu_{conj,side}$	mean Nusselt number averaged over the side wall for conjugate heat transfer
$Nu_{H2,bot}$	mean Nusselt number averaged over the bottom wall for H2 condition
$Nu_{H2,m}$	mean Nusselt number averaged over all peripheral walls for H2 condition
$Nu_{H2,side}$	mean Nusselt number averaged over the side wall for H2 condition
$Nu_{H2,top}$	mean Nusselt number averaged over the top wall for H2 condition
$Nu_{H2,x}$	longitudinal Nusselt number average over the perimeter of the wall
Pr	Prandtl number
$\overline{q''}_x$	average heat flux at axial location x (W/m^2)
Re	Reynolds number
SG103	channel for micro-PIV measurement with effective width at 103×10^{-6} m
SG34	channel for micro-PIV measurement with effective width at 34×10^{-6} m
SG53	channel for micro-PIV measurement with effective width at 53×10^{-6} m
St	Stanton number
$T_{m,x}$	fluid bulk mean temperature (K)
$\overline{T}_{W,x}$	axial wall temperature averaged over the perimeter of the wall
$u(X,t)$	velocity in the measurement volume as a function of space and time
$u(y)$	velocity distribution along y (m/s)
u_0	velocity at the centroid of the interrogation area (m/s)
u_m	mean velocity calculated in Eq. (2) (m/s)
$u_{wall}(y)$	velocity field extended to wall region as in Eq. (4) (m/s)
$W(X)$	weighting function
W_{c1}	width at the bottom of the channels (10^{-6} m)
W_{c2}	width at the top of the channel (10^{-6} m)
x	coordinates along the main flow direction
x^+	dimensionless distance from the inlet
X	3-D space coordinates vector
y	coordinates along the channel width direction
y_0	y coordinates at the centroid of the interrogation area
y_i	y coordinates at the boundary interfaces
z	coordinates along the channel depth direction
z_{max}	z coordinates of the plane with maximum velocity

Greek symbols

δz_{corr}	depth of correlation as in Eq. (1) (10^{-6} m)
ε	threshold defined as the ratio of the weighting function for the out-of-focus particles to that for the in-focus particles
λ	wavelength (10^{-9} m)

camera shutter, application of such a system is limited to very slow flow. A micro-PIV system capable of measuring over a broader range of velocity was described in Meinhart et al. [10]. Velocity distribution in a glass microchannel 30×10^{-6} m deep and 300×10^{-6} m wide were measured. A 5×10^{-9} s (5 ns) pulsed Nd:YAG laser was used as the light source to illuminate the 200×10^{-9} m diameter fluorescent particles. The images of the flow field were recorded using a $1300 \times 1030 \times 12$ bit CCD camera. The streamwise velocity profile estimated from the PIV measurements on one plane agreed within 2% with analytical results.

Recently, the effects of out-of-focus particles were examined in Meinhart et al. [11], Olsen and Adrian [12], and Bourdon et al. [13]. Olsen and Bourdon [14] and Olsen and Adrian [15] considered the effects of out-of-plane motions and Brownian motions. These works laid the foundation for applying the micro-PIV technique to characterize flow inside microchannels [5,16]. Park et al. [17] demonstrated confocal laser scanning microscopy (CLSM) can be used to improve the out-of-plane resolution. Mielnik and Sætran [18] showed that the out-of-focus resolution can be further improved using a selective-seeding technique to reduce the background noise caused by out-of-focus particles associated with volume seeding technique.

In this work, velocity distributions inside slightly tapered microchannels were directly measured using the non-intrusive micro-PIV technique. An image parity exchange technique developed by Tsuei and Savas [19] for macro-scale PIV was adapted to improve the accuracy in velocity measurement near the wall–fluid interface. The measured results agree well with theoretical predictions. It was found that the location of the maximum velocity deviates significantly from the mid-plane in the depth direction for the slightly tapered microchannel. Numerical simulations revealed that this effect increases as the sidewall

slope increases, and significant degradation in heat transfer can occur if considerable sidewall slope is present. Although measuring laminar flow inside microchannel has been reported elsewhere [4,5], the current study appears to be the first to explore the effects of the non-ideal channel profiles due to manufacturing using micro-PIV. At the same time, to the authors' knowledge, this study applies the micro-PIV technique to the smallest microchannel width (34×10^{-6} m) yet reported.

1. Fabrication of the microchannel

Fig. 1 shows the fabrication steps, mask layout and cross-section schematic of the silicon microchannel tested in this study. In Fig. 1a, steps (1)–(3) define the circular holes for the pressure taps and fluid inlet on the front side of the wafer, while steps (4) and (5) define the microchannel as well as the square header on the backside of the wafer. The process started with the deposition of a 0.9×10^{-6} m thick layer of SiO_2 on the backside of a double-polished silicon wafer. In the second step, 14×10^{-6} m thick positive photo-resist AZP 4620 was spun on the front side of the wafer and baked at 100 °C for 10 min on a hot plate. After a standard photo-lithography process in a Karl-Suss MA6 mask aligner (h-line), the exposed wafer was developed in 1:3 diluted AZ400K developer and subsequently rinsed and baked at 90 °C for 10 min. In step (3), the wafer was put in a Plasma-Therm ICP machine to etch the pressure tap and fluid inlet holes. The photo-resist was then removed in heated SHIPLEY MICROPOSIT remover 1165A and the SiO_2 was then stripped-off from the backside. After thorough cleaning in Piranha solution, PECVD SiO_2 was deposited on the front side of the wafer where holes had been defined in previous steps. The same processes for the holes were repeated to fabricate the microchannel on the backside, as listed in steps (4) and (5). A Pyrex 7740 glass wafer was finally bonded to the microchannel side of the wafer by anodic bonding, as shown in step (6). The mask layout for the microchannel is shown in Fig. 1b, where the first square from the left is for pressure measurement and the second square is for fluid inlet. Backside alignment was employed to ensure these two squares were aligned well with the two round holes on the other side of the wafer, shown as dashed lines. Fig. 1c illustrates the cross-sectional profile of the bonded microchannel. Although vertical sidewall is desired, deviations usually occur, the extent of which is determined by the channel aspect ratio, deposition pressure, etch time and RF power.

Fig. 2 shows the effects of the channel aspect ratio on the sidewall profile fabricated in a Plasma-Therm ICP machine for the current study. As can be seen, narrow and deep channel tends to be tapered and wide shallow channel tends to be re-entrant. The dimensions of the microchannels fabricated are listed in Table 1 and can be referred to Fig. 1c. The channels are labeled as SG (for *single* channel) followed by the effective width measured at the mid-point. As shown in Table 1, both channels SG34 and SG53 are slightly tapered, by about 0.5°. Vertical sidewall profile was only achieved for SG103, as can be seen from Fig. 3.

The channel dimensions were measured at 40 locations across the microchannels area using optical microscope for width measurement and Wyko optical profilometer for depth measurement. The uncertainty due to the optical microscope width measurement is estimated to be ±0.5 μm. The data scatter in width is around ±3%. For depth measurement, the calibration uncertainty for the Wyko profilometer is ±0.85%. The depth measurement uncertainty is estimated to be ±3%. The combined uncertainty for hydraulic diameter is ±4.4%.

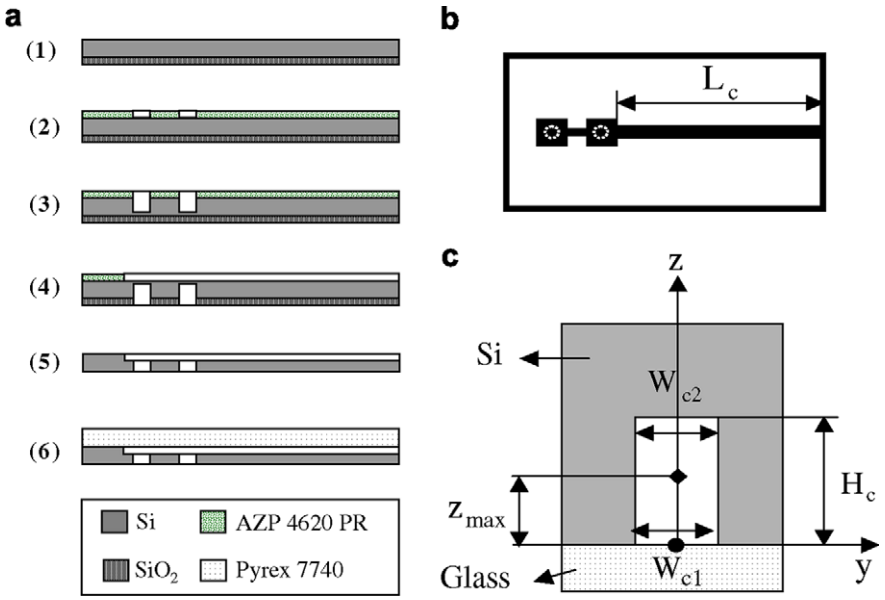

Fig. 1. (a) Fabrication steps for the microchannel, (b) mask layout of the microchannel and (c) schematic of the cross-section of the microchannel.

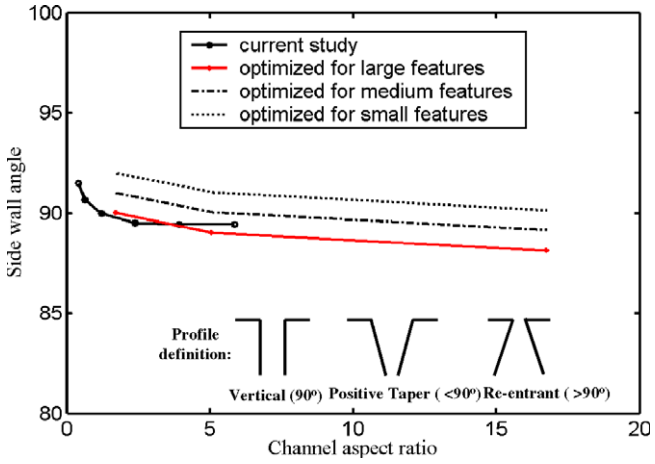

Fig. 2. Effects of channel aspect ratio on the sidewall profile.

Table 1
Dimensions of microchannels fabricated using DRIE (10^{-6} m)

	Channel		
	SG34	SG53	SG103
W_{c1}	35	54	103
W_{c2}	33	52	103
H_c	118	119	123
Sidewall taper (deg)	0.48	0.48	0

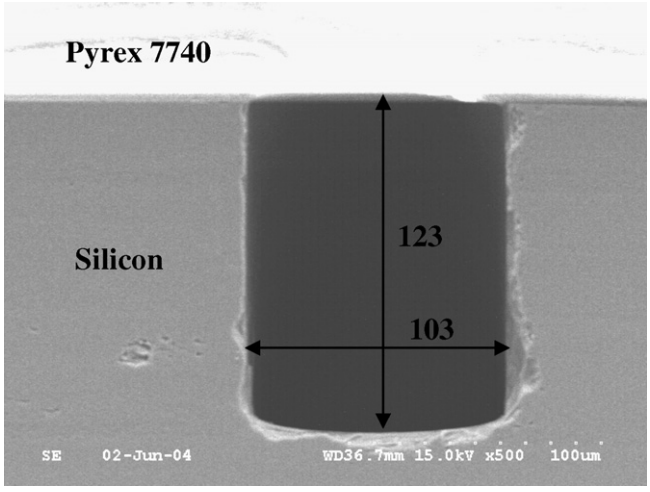

Fig. 3. Scanning electron micrograph of the cross-section of a bonded microchannel for micro-PIV. All dimensions are in 10^{-6} m (μm).

DRIE etching usually results in two types of surface roughness on the sidewalls of the microchannel [20]. One is the scallop pattern ($\sim 0.5 \times 10^{-6}$ m) due to the Bosch process. The other is the irregular vertical groves the dimension of which is process dependent. The causes of the latter are not well understood so far. For the current study, surface roughness is considered to have little effect, as the channel dimensions are much larger. Similar observations have been made in Baviere [21].

In this work, velocity profiles for SG34 were measured at different focus planes. Sidewall profile effects on the location of the maximum velocity for SG34, SG53 and SG103 were examined using micro-PIV. Numerical simulations were also conducted to further investigate sidewall profile effects on the flow and heat transfer characteristics for microchannels that have larger slopes than SG34 but otherwise have the same dimensions as SG34.

2. Experiment setup and procedures

The microchannels were tested in a setup schematically shown in Fig. 4. A micro-PIV system commercially available from DANTEC Inc. was used to measure the velocity field. The imaging system includes an epi-fluorescent inverted microscope (Nikon Eclipse TE2000-S), dual Nd:YAG lasers (Gemini PIV 200) and a cooled interline CCD camera. The epi-fluorescent filter cube consists of an excitation filter, a dichromatic mirror and an emission filter. The pulsed green light from the dual lasers expands through a beam expander, and passes through the diffuser, the excitation filter and the dichromatic mirror to the microscope objectives. Fluorescent particles (Nile Red, Molecular Probe) excited by this incident green light emit red light peaked around 560×10^{-9} m. The emitted red light passes through the long pass emission filter to reach the CCD camera, which operates in the double-frame single exposure mode. Scattered green light from the background and ambient is blocked at the emission filter.

A syringe pump capable of delivering flow rate of 0–2.78×10^{-9} m^3/s (0–10 ml/h) was used to drive the seeded solutions to the microchannels. Flow rate of the syringe pump was calibrated by weighing the mass changes over a period of time. The actual flow rate supplied by the syringe pump was within 3% of the nominal flow rate. At the beginning of each test, the image of channel wall boundary was aligned with the coordinates in the CCD sensor array by rotating the sample holder. A scale factor was determined as the ratio of the known physical size of the channel width to the image size in the CCD camera array. This

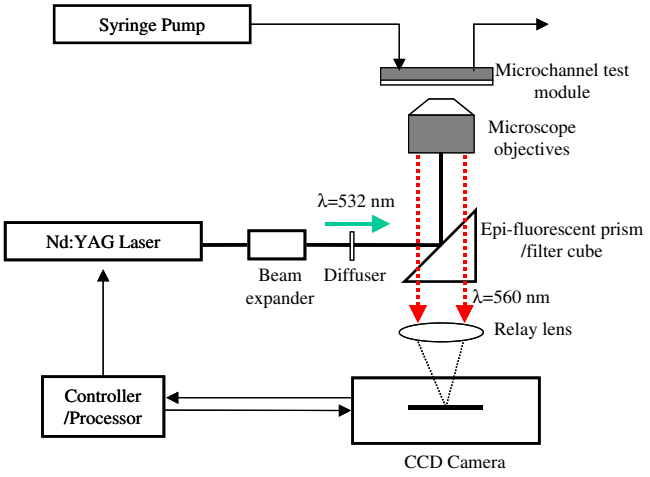

Fig. 4. Schematic of a micro-PIV test setup.

scale factor was used to obtain the actual displacement between two laser pulses.

Before taking images for velocity measurement, pressure drop was closely monitored for about 20 min until steady state was achieved. In this experiment, the measurement plane was always parallel to the top surface of the microchannels. By rotating the fine focus knob of the microcscope, which has 1 μm minimum dial, measurement plane (x–y) can be translated along z direction, as shown in Fig. 1c. Velocity measurement was thus obtained at different depths of the channel.

3. Considerations for micro-PIV measurement

The accuracy and spatial resolution of a micro-PIV measurement are determined by the hardware setup and the image and data processing techniques.

3.1. Seeding particles

For the current study, Nile-red epi-fluorescent particles were used. The particle diameter is 0.5×10^{-6} m and the specific gravity is 1.06. This results in a relaxation time on the order of 10^{-8} s [9]. The relative error due to Brownian motion for the current study, determined using the procedure of Santiago et al. [9], is typically less than 2%. This error can be further reduced by ensemble averaging over repeated measurements, as the diffusive error is inversely proportional to the square root of the size of the ensemble. Volumetric concentrations in the range of 0.05–0.07% were found to provide reasonable signal-to-noise ratio (SNR) when an ensemble averaging procedure described in Meinhart et al. [22] was performed over 40 consecutive realizations.

3.2. Spatial resolution and depth of measurement

The spatial resolution of any PIV measurement is defined by the size of the interrogation region and ultimately limited by the effective particle image size. The image of a finite-diameter particle is the convolution of the diffraction limited point response function with the geometric image of the particle [8]. In the present study a long working distance objective with magnification $M = 60$ and numerical aperture NA = 0.7 is used to resolve the 0.5×10^{-6} m particles. The effective image diameter is about 52×10^{-6} m, and it corresponds to 0.87×10^{-6} m when projected back to the flow field. The interrogation area used was 64 pixel in streamwise direction and 32 pixel in the transverse direction. This corresponds to spatial resolution of 7.3×10^{-6} m $\times$ 3.6×10^{-6} m. When 50% overlap was used for the interrogation, about 20 vectors were measured across the channel width of 34×10^{-6} m.

One important parameter in interpreting the velocity data is the depth of measurement, since the out-of-focus particles also contribute to the correlation function. Olsen and Adrian [12] derived the depth of correlation based on the assumption that the particle image intensity follows Gaussian distribution and the illumination over the interrogation area is uniform. The depth of correlation is given as

$$\delta z_{\mathrm{corr}} = 2\left[\frac{(1-\sqrt{\varepsilon})}{\sqrt{\varepsilon}}\left(f^{\#^2} d_{\mathrm{p}}^2 + \frac{5.95(M+1)^2\lambda^2 f^{\#^4}}{M^2}\right)\right]^{1/2} \tag{1}$$

where ε is a threshold defined as the ratio of the weighting function for the out-of-focus particles to that for the in-focus particles, $f^{\#}$ is the f-number of the optics, λ is the recording wavelength, d_{p} is the particle diameter and M is the magnification. Typically, ε is chosen as 0.01 [12]. For the current imaging system settings, Eq. (1) gives a measurement depth of about 2.65 μm.

3.3. Image processing and correlation analysis

In PIV, the measured velocity is defined by the particle image displacement divided by the product of the magnification and the time intervals. The measured velocity is essentially an average over the interrogation region and is assigned to the centroid of the interrogation area. Effectively the velocity is thus given by [12]

$$u_{\mathrm{m}} = \frac{\int u(X,t)W(X)\mathrm{d}X}{\int W(X)\mathrm{d}X} \tag{2}$$

where $W(X)$ is the weighting function which determines the relative contribution to the correlation function at different positions of the interrogation area. If the velocity is fully developed, it is only dependent on the y coordinates as shown in Fig. 5. The velocity within the interrogation area can be expanded into Taylor series around the centroid of the interrogation area

$$u(y) = u_0 + \left.\frac{\partial u}{\partial y}\right|_{y_0}(y-y_0) + \frac{1}{2}\left.\frac{\partial^2 u}{\partial y^2}\right|_{y_0}(y-y_0)^2 + \mathrm{O}(y-y_0)^3 \tag{3}$$

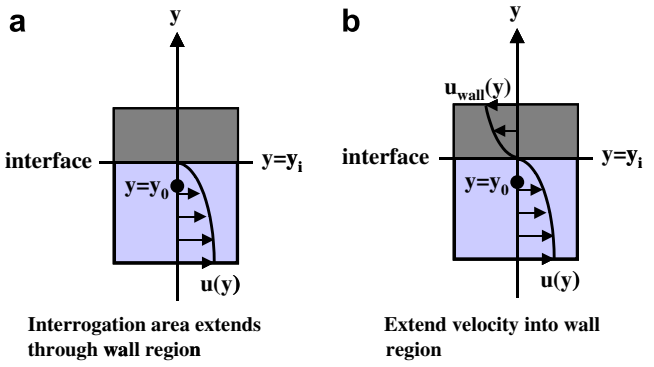

Fig. 5. Effects of the presence of wall boundary inside interrogation area on the velocity measurement.

where u_0 is the true velocity at the centroid. Clearly, the velocity is biased when there is a velocity gradient within the interrogation area. If a uniform weighting function is used the measurement bias is the second order as the first-order term is terminated during the integration across the interrogation area.

If the interrogation area extends beyond the wall boundary, however, additional large bias in the velocities will occur. The largest bias occurs when the centroid of the interrogation area is located on the solid–liquid interface. As the velocity should be zero for the no-slip boundary condition, a non-zero velocity will be measured as only half of the interrogation area contributes to the correlation function. This issue could be addressed if the velocity field can be extended to the wall area according to Eq. (4), which is proposed by Tsuei and Savas [19] for macro-scale PIV.

$$u_{\text{wall}}(y) = 2u(y_i) - u(2y_i - y) \tag{4}$$

where y is the coordinate orthogonal to the flow direction, as shown in Fig. 5, y_i is the location of the interface.

A Taylor series expansion around the centroid reveals that the extension in Eq. (4) is accurate to the first order; consequently using Eq. (4) improves the accuracy near the boundary region to the same degree for the bulk fluid region. Implementation of Eq. (4) is straightforward. With reference to Fig. 5, point y in the wall region and point $(2y_i - y)$ inside the channel are symmetric about the interface located at y_i. Since the interface velocity $u(y_i)$ is zero for the no-slip boundary condition, Eq. (4) indicates a reflection and a reverse of the velocity field inside the channel about the interface. This is achieved through the image process steps illustrated in Fig. 6 such that images for both frames are reflected about the interface. The wall region of the second frame is replaced with the reflected image of the fluid region in the first frame and vice versa. This process is referred to as image parity exchange (IPX) in [19] and will be used hereafter. In micro-PIV measurement, the wall boundary is usually hard to define as it blurs as a result of defocusing. In the present study, a Matlab function which searches for the maximum image intensity gradient is used to locate the channel boundary.

It is noted here that before the IPX process mean pixel intensity value is subtracted from the raw image maps to reduce the background noise. To identify the effects of IPX, correlation analysis is also performed on the image maps where only mean intensity is subtracted. These results are compared with predicted velocity profiles from the series solution for rectangular channel [23] and numerical solution for trapezoidal channel. As can be seen from Fig. 7 applying IPX before the correlation significantly improves the accuracy of the velocity profile prediction near the wall. This is particularly useful for measuring velocity for very narrow channels where boundary effects are significant such as the channel sizes in the current study.

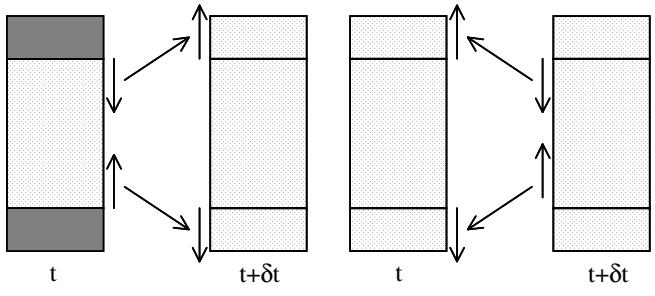

Fig. 6. Implementation of Eq. (4) to extend the velocity field to the wall region.

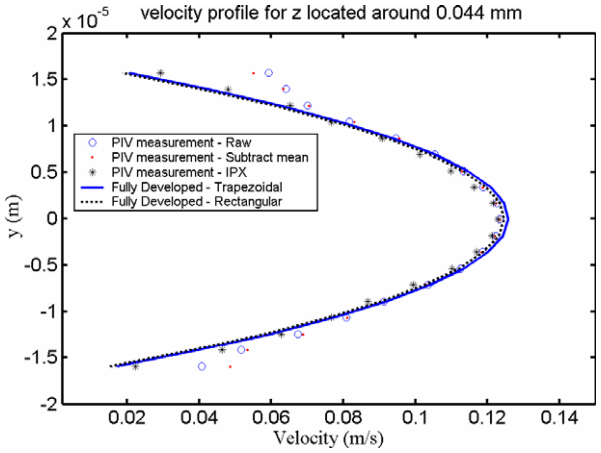

Fig. 7. Velocity profile using different image processing techniques.

Following the procedures described in previous sections, images at different focus planes were recorded and processed for correlation analysis. Since the flow is steady, an ensemble average technique can be used to enhance the SNR as described in Meinhart et al. [22]. To determine the velocity vectors, adaptive correlation was first conducted to the image maps. The average velocity map obtained was then used as the offset for the ensemble average correlation. This offset was applied to reduce the loss-of-pair issue successfully.

4. Results and discussion

4.1. Velocity profiles for fully developed flow

Figs. 8 and 9 plot the velocity profile for SG34 at different z planes for the flow rate of 2.78×10^{-10} m^3/s (1 ml/h) and 1.11×10^{-9} m^3/s (4 ml/h) respectively. Predicted results based on analytical solutions for an effective rectangular channel and numerical simulations for a trapezoidal channel are plotted for comparison. As can be clearly seen, the measured velocity profile matches very well with results predicted from laminar theory for all the planes measured. Even though the actual channel is not perfectly trapezoidal, the trapezoidal model results generally agree better with experimental measurements than the rectangular model, particularly for the measurement plane located away from the geometric symmetry plane. These comparisons clearly prove the validity of the laminar theory for microchannels.

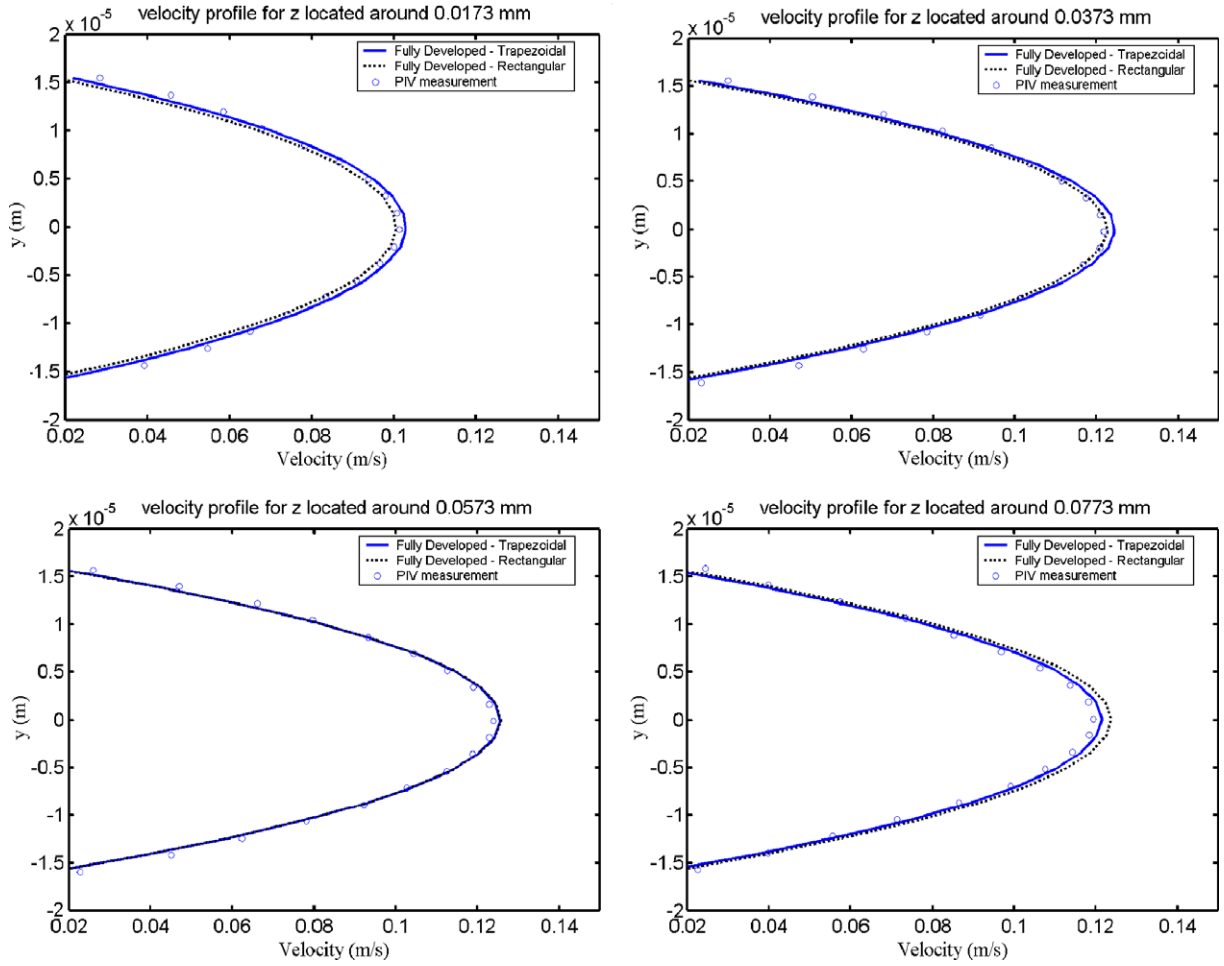

Fig. 8. Velocity profile at different focus planes (flow rate 2.78×10^{-10} m^3/s or mean velocity 0.07 m/s).

These results also confirm the feasibility of using micro-PIV as a diagnostic tool for microfluidics for channels of these sizes.

4.2. Developing flow near entrance

Fig. 10 presents results measured near the entrance of the SG103 channel. A typical velocity vector is shown in Fig. 10a. In the manifold the flow is slow and subsequently accelerated upon entering the channel. At the beginning the velocity is nearly uniform and an approximately parabolic profile establishes after about 0.1 mm from the entrance. Fig. 10b shows the mean velocity average along y-direction at the z-plane. As the flow approaches fully developed condition, the mean velocity for this plane stabilizes. The non-dimensional hydrodynamic developing length is determined to be 0.091 after which the variations of the mean velocity are within one percent of the fully developed value. This result matches very well with the result reported in [23].

4.3. Effects of the sidewall profile on flow and heat transfer

As shown in Table 1, the sidewalls of SG34 and SG53 deviate by 0.5° from vertical while the sidewall of SG103 is vertical. The effects of the sidewall profiles on the velocity fields for these microchannels were examined through micro-PIV measurements. Numerical models were also developed to characterize the flow and heat transfer inside microchannels with larger slopes, which are realistic scenarios as reported in [6,7]. A commercial software package FLUENT 6.0 was used for this purpose. Conservation equations of mass, momentum and energy were solved using the built-in multi-grid solver. It uses a control-volume-based technique to discretize the equations into algebraic equations. The pressure–velocity coupling is handled using SIMPLE algorithm [24]. For comparison, the flow rate, channel depth and opening width are kept the same as SG34 for these numerical modeling studies. Effects of boundary condition and boundary layer development were also explored.

4.3.1. Flow

Deviations from rectangular cross-section (90° side wall) cause deviations in velocity profiles. This effect can be quantified by looking at z_{max}, the vertical location of the maximum velocity over the cross-section, as defined in Fig. 1c. Table 2 lists the results of z_{max} from micro-PIV measurement for the channels listed in Table 1 and com-

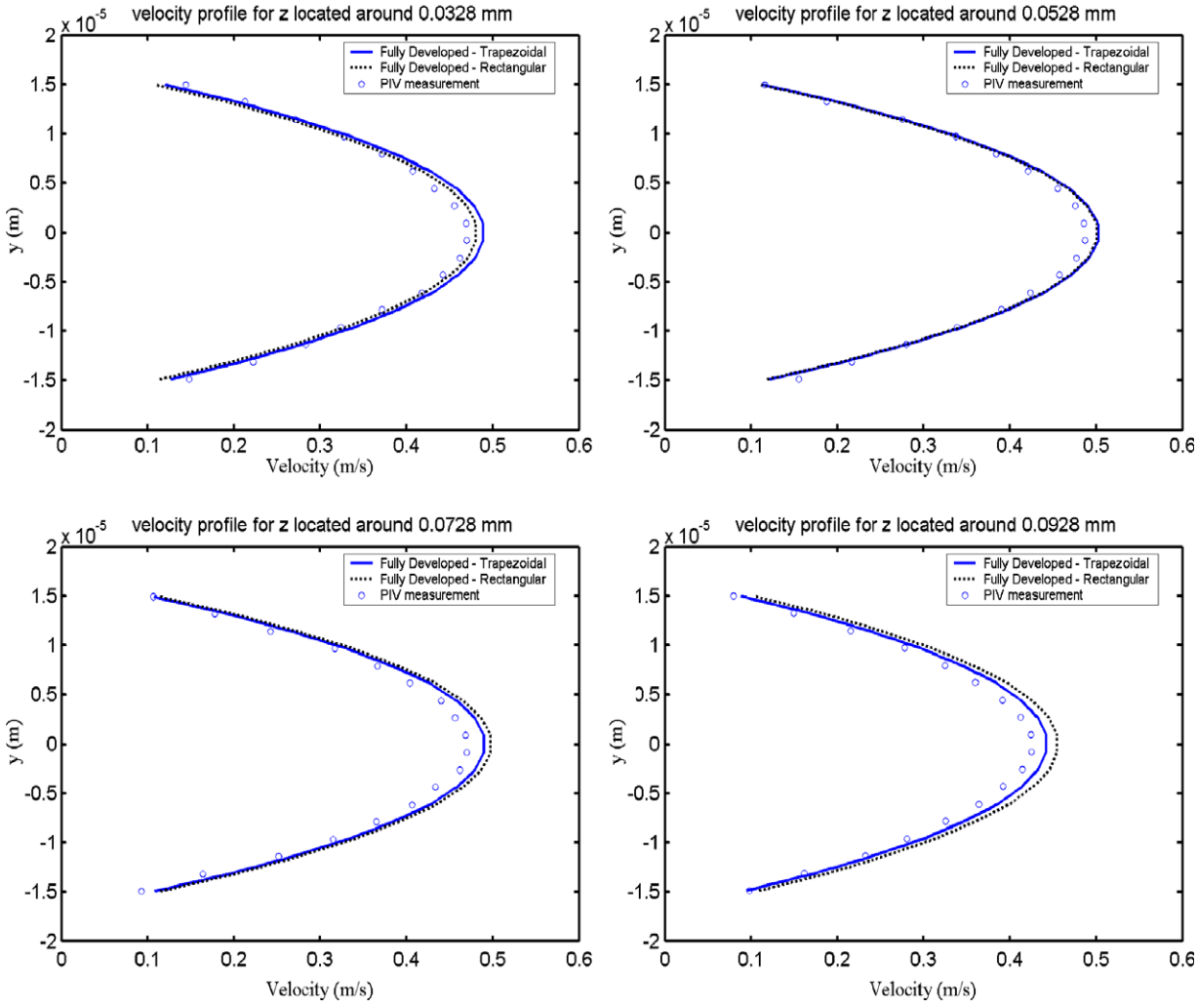

Fig. 9. Velocity profile for SG34 (1.11×10^{-9} m^3/s or 0.28 m/s).

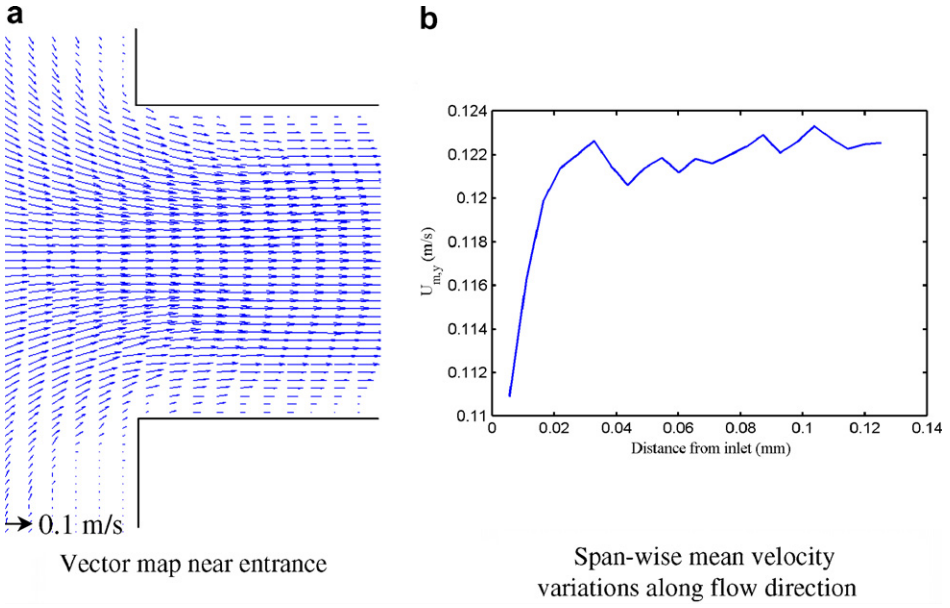

Fig. 10. Velocity profile development for SG103 ($Re = 9.8$).

pares them with model predictions for rectangular and/or trapezoidal channels.

If the channel cross-section is rectangular then the velocity profile should be symmetric about $z = 0.5H_c$. For SG34 the z_{max} difference between micro-PIV measurements and rectangular assumptions is about 20%. This is rather significant, considering that the channel cross-section taper is only 0.5°. Further modeling results from numerical simulation of trapezoidal channels agree well with the measured results from micro-PIV. If the maximum velocity plane were assumed as the symmetric plane and used as a reference to compare with the PIV measurement, large discrepancies would occur.

For wider channels SG53 and SG103 numerical modeling reveals that the locations of the maximum velocity are very close to the mid-point of the channel depth. This is also confirmed in micro-PIV measurement results, as shown in Table 2.

Clearly, these results indicate that the effect of the sidewall profile is very significant for channels of large aspect ratio. This effect should be considered when designing microchannel heat exchangers or micro-reactors, as channels of large aspect ratio are usually desired for these applications [25].

Keeping the flow rate, channel depth and opening width the same as SG34, numerical simulations were carried out to characterize the flow and heat transfer for microchannels with larger sidewall slope. Grid sensitivity study was conducted and a grid system of $40 \times 40 \times 100$ was used finally. As the sidewall slope increases, the effects of sidewall slope become even more dramatic. Fig. 11 indicates that the shift of maximum velocity plane from mid-point of the channel depth increases significantly with the angle. For a 5° angle, the plane of maximum velocity is located at almost one-fifth of the total depth from the bottom of the channel, while 72% of the total flow rate passes the lower half cross-section.

One key parameter of microchannel flow is the pressure drop. Fig. 12 indicates for the fixed bottom width and channel depth, as the angle increases, the pressure drop increases due to the smaller flow area. For each angle, the ratio between the friction factor for the trapezoidal channel and that for corresponding rectangular channel is generally smaller than one. This means for the same flow area trapezoidal channel has less friction loss. This reduction in friction loss is about 7% for a 5° angle. For small angles, this effect is minimal.

Table 2
Locations of the plane with maximum velocity z_{max} (10^{-6} m)

	Flow rate (ml/h)		
	1	4	10
SG34			
Micro-PIV	50.8	46.2	48.5
Rectangular model	59	59	59
Trapezoidal model	48.5	48.5	48.5
SG53			
Micro-PIV	57	N.A.	N.A.
Rectangular model	59.5	N.A.	N.A.
Trapezoidal model	59.5	N.A.	N.A.
SG103			
Micro-PIV	N.A.	61.9	58
Rectangular model	N.A.	61.5	61.5

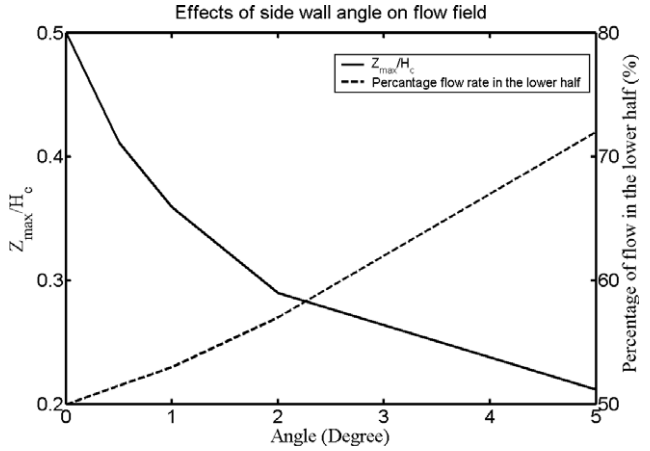

Fig. 11. Angle effects on flow characteristics.

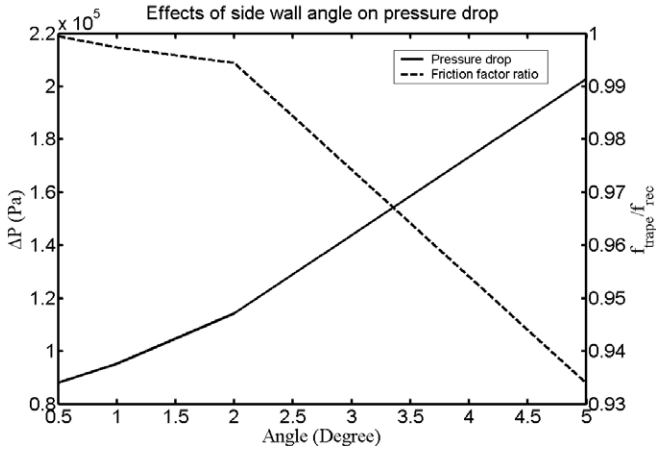

Fig. 12. Effects of sidewall angle on friction losses. Pressure drops are for trapezoidal channel, while friction factor ratio is the ratio between the trapezoidal and the corresponding rectangular channel with equal flow area.

4.3.2. Heat transfer

Numerical modeling was conducted for trapezoidal channel with 5° sidewall slope. Constant heat flux condition was assumed at all four walls. This is also referred as the H2 condition in Shah and London [23]. To evaluate the impact of the side wall profile on the heat transfer characteristics, the longitudinal heat transfer and Nusselt numbers are defined in Eqs. (5) and (6), which are consistent with the definitions in Shah and London [23]. For fully developed conditions, the predicted Nusselt numbers from current study agree well with results reported in Shah and London [23], which also validates the modeling technique.

As shown in Table 3, compared with rectangular channels of the same flow area, Nusselt number for a tapered channel is significantly lower. At fully developed condition, the degradation in Nusselt number is about 60%. It is interesting that near the entrance this degradation is not as significant because there the boundary layer development just starts and the velocity and temperature profiles over the majority of the cross-section are rather close to uniform

$$\bar{h}_x = \frac{\overline{q''}_x}{\overline{T}_{W,x} - T_{m,x}} \tag{5}$$

$$Nu_{H2,x} = \frac{\bar{h}_x d_H}{k_f} \tag{6}$$

Fig. 13 shows temperature contours at the cross-sections of a rectangular channel and a trapezoidal channel with 5° sidewall slope. Clearly, temperature gradient along the side wall of the trapezoidal channel is much steeper than the rectangular channel. As the flow core area shifts towards the bottom, the heat transfer efficiency of the upper half of the channel decreases significantly. As constant heat flux boundary conditions are applied, temperatures near the upper corners are significantly higher. Near the bottom, heat transfer is enhanced due to much thinner boundary layers. However, the overall heat transfer for a trapezoidal channel is significantly lower as heat transfer degradation for side wall and top wall dominates any heat transfer enhancement for bottom wall. This is clearly shown in Fig. 14, which shows the impact of the sidewall profile on

Table 3
Local Nusselt number for 5° trapezoidal channel and rectangular channel

	$\frac{x}{d_H \cdot Re \cdot Pr}$				
	0.09	0.18	0.45	0.85	Fully developed
$Nu_{H2,x}$ rectangular	3.89	3.44	3.09	2.96	2.94
$Nu_{H2,x}$, 5° sidewall	2.7	2.09	1.56	1.35	1.21
Degradation in *Nu* (%)	30	40	50	54	60

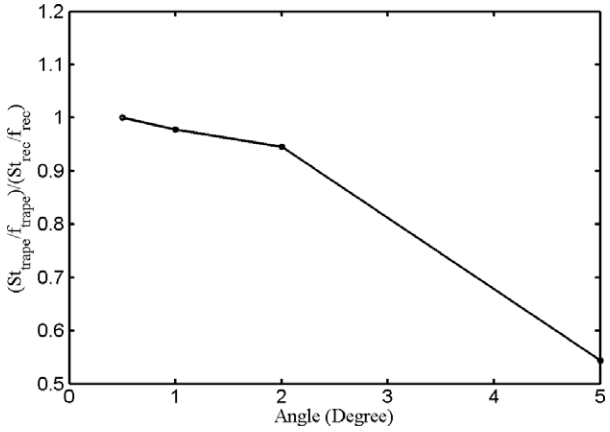

Fig. 14. Heat transfer performance variations with sidewall angle, H2 boundary condition.

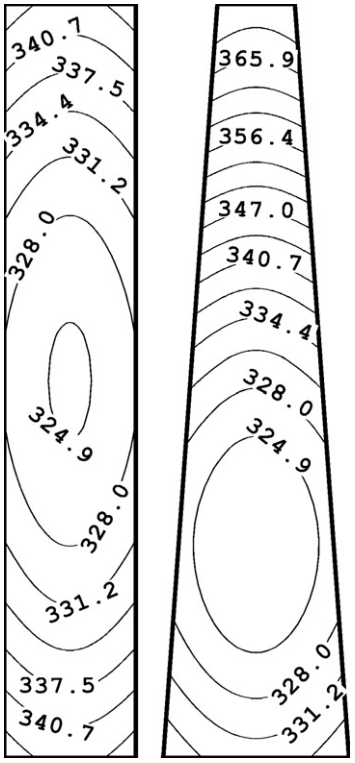

Fig. 13. Contour map of temperature (K) at the cross-section of rectangular and trapezoidal channel with 5° sidewall angle for H2 boundary condition.

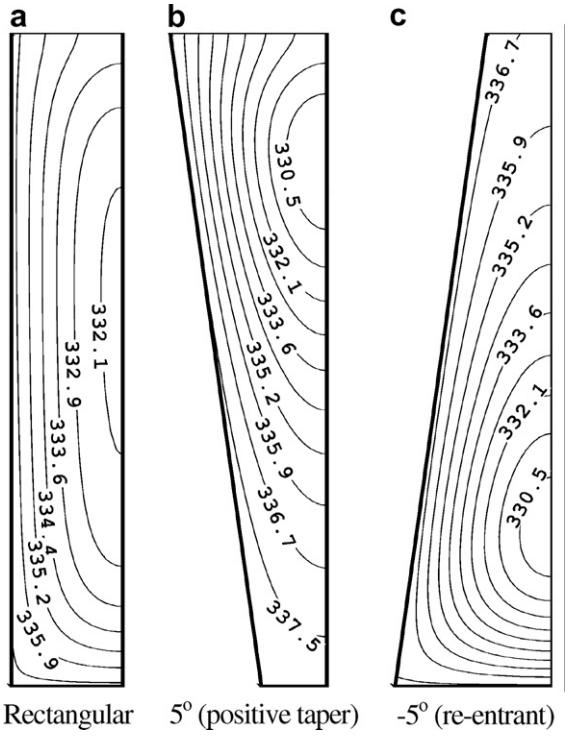

Fig. 15. Contour map of temperature (K) at the cross-section of channels with conjugate heat transfer (only half of the fluid cross-section is shown). Uniform heat flux is applied at bottom of the silicon and the top surface is adiabatic.

the heat transfer performance parameter. This ratio lumps the effects of heat transfer degradation and pressure drop reduction due to the presence of sidewall slope. Here St is the Stanton number defined in Eq. (7) and f is the friction factor

$$St = \frac{Nu}{RePr} \tag{7}$$

Constant heat flux condition is an idealized boundary condition which usually implies uniform heating of solid materials with low thermal conductivity. For applications such as micro-heat-exchangers, heat transfer is usually conjugate as the highly conductive solid region also participates in heat transfer.

Numerical modeling was conducted for conjugate heat transfer inside microchannels. To simulate the practical application conditions such as those in electronic cooling, uniform heat flux condition was applied at the bottom of the silicon region while the interface of the channel and glass was assumed adiabatic. It is noted here that the orientation used in this section is opposite to Fig. 1c such that silicon channels are at the bottom while sealing glass plate is at the top. Three different cases were studied in which the channel profiles were rectangular, positively tapered and re-entrant respectively. Fig. 15 depicts the temperature distribution across the fluid region only. Only half of the channel is shown due to the symmetry conditions. In sharp contrast to the H2 condition, temperature along the side and bottom walls are almost uniform for all three cases as the temperature contours are nearly parallel to the boundaries. This is clearly due to the high thermal conductivity of silicon (~148 W/mK at room temperature). Compared with rectangular channel in Fig. 15a, cold cores for positively tapered channel in Fig. 15b and re-entrant channel in Fig. 15c shift towards top and bottom respectively. Consequently, heat transfer near lower left corner of the tapered channel and upper left corner of the re-entrant channel are significantly reduced.

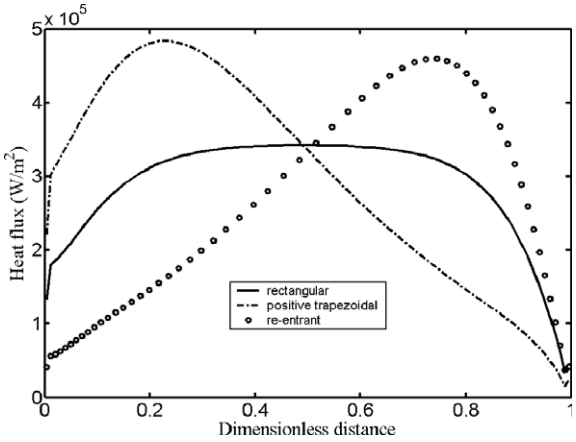

Fig. 16. Heat flux distribution along the sidewalls of all three channels.

As the solid silicon region surrounding the channels is very conductive, more heat is dissipated near the cold core area. This is clearly shown in Fig. 16. Therefore, the overall degradation in heat transfer for conjugate heat transfer is much less as is shown in Table 4. It is interesting that for conjugate heat transfer, re-entrant channel is more efficient than a positively tapered channel. There are two reasons for this. As the top wall is adiabatic, the total heat transfer area for re-entrant channel is slightly larger. More importantly, the bottom wall of the re-entrant channel contributes more efficiently to heat transfer as the boundary layer is much thinner, while for the positively tapered channel this contribution is much less. As indicated in Table 4, mean Nusselt number for bottom wall is 2.93 for the re-entrant channel and 0.6 for the positively tapered case.

5. Summary and conclusion

In summary, direct measurement of velocity field inside silicon microchannels were conducted using micro-PIV. An image parity exchange technique for macro-scale PIV was adapted to reduce the bias in the near wall region. The effects of sidewall slope due to micro-fabrication defects were examined experimentally by micro-PIV and numerically by simulation. For channels with large aspect ratio, even 0.5° slope in channel sidewall can cause 20% deviation on the location of the maximum velocity. Results from micro-PIV measurements closely agree with numerical simulation. Numerical simulations were also carried out to study the effects of the sidewall profile on the heat transfer. For constant heat flux condition, serious degradation in overall heat transfer occurs for channel with 5° slope. For conjugate heat transfer, the degradation in heat transfer is much less and re-entrant channel has better heat transfer performance than positively tapered channel. It is concluded that for microchannels with large aspect ratio the transport characteristics are very sensitive to the channel profiles; therefore, careful design and control of the microfabrication process are crucial to the performance of the micro-scale devices.

Table 4
Nusselt numbers for rectangular, positively tapered and re-entrant channels for H2 boundary condition or conjugate heat transfer ($x^+ = 0.45$)

Angle (deg)	$Nu_{H2,m}$	$Nu_{conj,m}$	$Nu_{H2,side}$	$Nu_{conj,side}$	$Nu_{H2,bot}$	$Nu_{conj,bot}$	$Nu_{H2,top}$
0	3.05	5.19	4.43	5.58	1.13	2.02	1.13
−5	1.56	4.13	1.69	4.33	0.41	2.93	4.56
5	1.56	3.93	1.69	4.18	4.56	0.6	0.41

Acknowledgements

The authors acknowledge support for this work under the DARPA HERETIC Program through contract N00164-99-C-0039, managed by Drs. Elias Towe, Dan Radack and Christie Marrian. We also appreciate support from Intel corporation and Dr. Michael Patterson.

References

[1] J. Judy, D. Maynes, B.W. Webb, Characterization of frictional pressure drop for liquid flows through microchannels, Int. J. Heat Mass Transfer 45 (17) (2002) 3477–3489.
[2] T.M. Harms, M.J. Kazmierczak, F.M. Gerner, Developing convective heat transfer in deep rectangular microchannels, Int. J. Heat Fluid Flow 20 (2) (1999) 149–157.
[3] H.Y. Wu, Ping Cheng, Friction factors in smooth trapezoidal silicon microchannels with different aspect ratios, Int. J. Heat Mass Transfer 46 (14) (2003) 2519–2525.
[4] L. Zhang, J.M. Koo, L. Jiang, M. Asheghi, K.E. Goodson, J.G. Santiago, T.W. Kenny, Measurement and modeling of two-phase flow in microchannels with nearly constant heat flux boundary conditions, J. Microelectromech. Syst. 11 (1) (2002) 12–19.
[5] S. Devasenathipathy, J.G. Santiago, S.T. Wereley, C.D. Meinhart, K. Takehara, Particle imaging techniques for microfabricated fluidic systems, Exp. Fluids 34 (4) (2003) 504–514.
[6] A.A. Ayón, R.A. Braff, C.C. Lin, H.H. Sawin, M.A. Schmidt, Characterization of a time multiplexed inductively coupled plasma etcher, J. Electrochem. Soc. 146 (1) (1999) 339–349.
[7] A.A. Ayón, R.A. Braff, R. Bayt, H.H. Sawin, M.A. Schmidt, Influence of coil power on the etching characteristics in a high density plasma etcher, J. Electrochem. Soc. 146 (7) (1999) 2730–2736.
[8] R.J. Adrian, Particle imaging techniques for experimental fluid mechanics, Ann. Rev. Fluid Mech. 23 (1991) 261–304.
[9] J.G. Santiago, S.T. Wereley, C.D. Meinhart, D.J. Beebe, R.J. Adrian, A particle image velocimetry system for microfluidics, Exp. Fluids 25 (4) (1998) 316–319.
[10] C.D. Meinhart, S.T. Wereley, J.G. Santiago, PIV measurements of a microchannel flow, Exp. Fluids 27 (5) (1999) 414–419.
[11] C.D. Meinhart, S.T. Wereley, M.H.B. Gray, Volume illumination for two-dimensional particle image velocimetry, Meas. Sci. Technol. 11 (6) (2000) 809–814.
[12] M.G. Olsen, R.J. Adrian, Out-of-focus effects on particle image visibility and correlation in microscopic particle image velocimetry, Exp. Fluid 29 (7) (2000) 166–174.
[13] C.J. Bourdon, M.G. Olsen, A.D. Gorby, Validation of an analytical solution for depth of correlation in microscopic particle image velocimetry, Meas. Sci. Technol. 15 (2004) 318–327.
[14] M.G. Olsen, C.J. Bourdon, Out-of-plane motion effects in microscopic particle image velocimetry, J. Fluids Eng. 125 (5) (2003) 895–901.
[15] M.G. Olsen, R.J. Adrian, Brownian motion and correlation in particle image velocimetry, Optics Laser Technol. 32 (7) (2000) 621–627.
[16] D. Liu, S.V. Garimella, S.T. Wereley, Infrared micro-particle image velocimetry of fluid flow in silicon-based microdevices, in: 2004 ASME Heat Transfer/Fluids Engineering Summer Conference, Charlotte, NC, Paper number HT-FED04-56385.
[17] J.S. Park, C.K. Choi, K.D. Kihm, Optically sliced micro-PIV using confocal laser scanning microscopy (CLSM), Exp. Fluids 37 (1) (2004) 105–119.
[18] M.M. Mielnik, L.R. Sætran, Improvement of micro-PIV resolution by selective SEEDING, in: Proceedings of ICNMM2006 Fourth International Conference on Nanochannels, Microchannels and Minichannels, June 19–21, 2006, Limerick, Ireland, Paper number ICNMM2006-96146.
[19] L. Tsuei, O. Savas, Treatment of interfaces in particle image velocimetry, Exp. Fluids 29 (3) (2000) 203–214.
[20] Hongseok Noh, Parylene Microcolumn for Miniature Gas Chromatograph, PhD thesis, Georgia Institute of Technology, Atlanta, GA, 2004.
[21] R. Baviere, F. Ayela, S.Le. Person, M. Favre-Marinet, An experimental study of water flow in smooth and rough rectangular microchannels, in: 2nd International Conference on Microchannels and Minichannels, Rochester, NY, 2004, pp. 221–228.
[22] C.D. Meinhart, S.T. Wereley, J.G. Santiago, A PIV algorithm for estimating time-averaged velocity fields, J. Fluids Eng. 122 (2) (2000) 285–289.
[23] R.K. Shah, A.L. London, Laminar Flow Forced Convection in Ducts, Academic Press, New York, 1978, p. 200.
[24] S.V. Patankar, Numerical Heat Transfer and Fluid Flow, Hemisphere Publishing, 1980.
[25] X.J. Wei, Y.K. Joshi, Stacked microchannel heat sinks for liquid cooling of microelectronic components, ASME Trans. J. Electron. Packaging 126 (1) (2004) 60–66.